AGU PUBLICATIONS

JGR

Journal of Geophysical Research: Atmospheres

RESEARCH ARTICLE
10.1002/2015JD024000

Key Points:
- Monte Carlo model is used to examine the sensitivity of the UV erythemal radiation enhancement
- The model produced satisfactory results when compared with UVER enhancement for Valencia
- Fractional cloud cover and cloud thickness influences the enhancement

Correspondence to:
J. A. Martínez-Lozano,
jmartine@uv.es

Citation:
Núñez, M., M. J. Marín, D. Serrano, M. P. Utrillas, K. Fienberg, and J. A. Martínez-Lozano (2016), Sensitivity of UVER enhancement to broken liquid water clouds: A Monte Carlo approach, *J. Geophys. Res. Atmos.*, *121*, 949–964, doi:10.1002/2015JD024000.

Received 27 JUL 2015
Accepted 29 DEC 2015
Accepted article online 4 JAN 2016
Published online 30 JAN 2016

©2016. American Geophysical Union. All Rights Reserved.

Sensitivity of UVER enhancement to broken liquid water clouds: A Monte Carlo approach

M. Núñez[1], M. J. Marín[2], D. Serrano[3], M. P. Utrillas[3], K. Fienberg[1], and J. A. Martínez-Lozano[3]

[1]School of Geography and Environmental Studies, University of Tasmania, Hobart, Tasmania, Australia, [2]Solar Radiation Group, Departament de Matemàtiques per a l'Economia i l'Empresa, Universitat de València, Valencia, Spain, [3]Solar Radiation Group, Departament de Física de la Terra i Termodinàmica, Universitat de València, Valencia, Spain

Abstract The study uses a Monte Carlo radiative transfer model to examine the sensitivity of the UV erythemal radiation (UVER) enhancement to broken liquid water clouds of the cumulus and stratocumulus type. The model uses monochromatic radiation at 310 nm corresponding approximately to the peak of the product between irradiance and the erythemal curve. All scattering, absorption, extinction coefficients, and spectral albedos are tuned to this wavelength. In order of importance, fractional cloud cover, the area of individual cloud patches, and cloud thickness exert a strong influence on the enhancement, with smaller contributions from cloud optical depth, cloud base height, and solar zenith angle. In order to produce realistic enhancements for our study area located in the Valencia region of Spain (39°30′N, 0°25′W), measurements were obtained from a Landsat image of the region in combination with a spectral Fourier transform model. The Monte Carlo model, as applied to the Fourier transform cloud distribution, produced satisfactory results compared to 1 year of measured UVER enhancement for the study region provided that fractional cloud cover was equal to or greater than 3/10. At smaller cloud fractions, the neglect of cloud patches less than 50 m × 50 m in area by the model created significant discrepancies.

1. Introduction

In the last few decades there have been numerous experimental studies that document how measured UV irradiances in cloudy environments are enhanced above cloudless values [*Alados et al*., 2000; *Calbó et al*., 2005; *Esteve et al*., 2010]. They are believed to originate as a result of reflection from cloud sides, but the underlying factors influencing the results are many, and in this study we have taken a modeling approach to examine how the enhancement responds as a function of a range of variables.

In almost all studies cloud effects are treated using a cloud modification factor (CMF), defined as the ratio of measured UV irradiance (erythema irradiance, UVB, or UVA) to an equivalent cloudless irradiance with the same zenith angle and background atmospheric conditions [*Calbó et al*., 2005]. Enhancement (ENH) occurs when CMF is greater than 1, which may be expressed as a percentage, ENH = (CMF − 1) 100. Reported estimates of ENH range from a maximum of over 8% to 30% for integrated UV band measurements [*Bordewijk et al*., 1995; *Schafer et al*., 1996; *Sabburg and Wong*, 2000]. The low figure of 8% was reported by *Sabburg and Wong* [2000] as representing a true enhancement after allowing for an uncertainty maximum of 32% and a measured CMF of 1.40.

The above figures represent instantaneous measurements, and it is expected that in most cases temporal averaging will reduce ENH given the stochastic nature of cloud structure and composition at a local level. Thus, *Mims and Frederick* [1994] and *McCormick and Suehrcke* [1990] report ENH between 10% and 20% for integration times of approximately 30 min and 3 h, respectively, while yearly averages of ENH of under 5% are reported for various cities in Spain [*Alados-Arboledas et al*., 2003]. Frequency of enhancement (FE) as a percentage of total CMF episodes has also been used in the literature, ranging from relatively high values of 25% reported by *Lubin and Frederick* [1991] to 2–3% above a measurement uncertainty threshold [*Sabburg and Wong*, 2000; *Sabburg and Calbó*, 2009].

The above studies examine how CMF varies in response to various environmental factors, mainly solar zenith angle, cloud cover, and cloud type [*Blumthaler et al*., 1994; *Thiel et al*., 1997; *Kuchinke and Núñez*, 1999; *Sabburg and Wong*, 2000; *Foyo-Moreno et al*., 2003; *Sabburg and Calbó*, 2009, amongst others]. Modeling studies by *Bodecker and McKenzie* [1996] and *Grant and Heisler* [2000] partition surface irradiance as a contribution from a cloudy and cloudless portion of the sky but neglect contributions from cloud sides.

More detailed studies of the scattering processes argue that enhancement is mainly a response to reflection from sides in cumulus-type clouds, the process leading to enhanced diffuse radiation [*Krzyscin et al*., 2003; *Lovengreen et al*., 2005]. Conversely, other studies have also reported a high incidence of cirriform clouds with the enhancement [*Kuchinke and Núñez*, 1999; *Sabburg and Calbó*, 2009], with the process being related to a lower zenith angle in scattered diffuse radiation from the cloud compared to the incident radiation [*Pfister et al*., 2003; *Sabburg and Calbó*, 2009] or from a combination of cirrus/cumulus cloud effects [*Parisi et al*., 2004].

From the above discussion, questions still remain about the relative importance of cloud sides versus cloud structure and compositions in the enhancement process. The role of cumulus versus cirrus clouds in the enhancement process is still unclear. In this study we use a three-dimensional Monte Carlo radiative transfer model (MCRTM) which is specially suited to the nature of radiation enhancement by clouds [*Iwabuchi*, 2006]. Furthermore, the sensitivity of enhancement to a range of cloud variables and solar zenith angle can be easily examined. To confine the problem further, only low-level liquid water clouds of the cumulus or stratocumulus clouds are only considered.

In this study we examine the enhancement characteristics of UV erythemal radiation (UVER) data collected in the Valencia region of Spain over a 1 year period in 2011 and its response to a range of variables. Additionally, the above mentioned Monte Carlo radiative transfer model is used to compare measured trends to those estimated by the model. In our configuration the model is not used as a predictive tool but rather as a guide to indicate expected magnitudes, relevant trends, and as means of filtering relevant from nonrelevant variables.

2. Methodology

2.1. Instrumentation

Experimental data were collected over a 1 year period on the roof of the Faculty of Physics building in the Burjassot campus of the University of Valencia, Spain (39°30′N, 0° 25′W; 30 m above sea level). Measurements of UVER were taken using a broadband UVB-1 radiometer by Yankee Environmental Systems (YES). Concurrent with these measurements, fish eye lens images were collected using a sky camera by Sieltec Canarias S. L. that allowed a visual characterization of fractional cloud cover and cloud type. Ancillary data on aerosol optical depth and aerosol properties were also collected using CE-318 CIMEL Sun photometer which formed part of the Aerosol Robotic Network of sensors [*Holben et al*., 1998].

The radiometer YES-UVB-1 was calibrated in the National Institute for Aerospace Technology at El Arenosillo, Spain. This standard calibration consists of a measurement of the spectral response of the radiometer indoors and a comparison with a Brewer MKIII spectroradiometer outdoors [*Vilaplana et al*., 2006]. It is estimated that the calibration provides a corrected signal with a maximum error of 9% for zenith angles below 70° [*Utrillas et al*., 2007; *Núñez et al*., 2011]. The UVER data were acquired at 5 min intervals using an Agilent 34970A data logger.

Cloud sky images were acquired simultaneously at 5 min intervals, stored on local memory, examined, and downloaded if the images were deemed suitable. The web software allowed rapid scanning of the images which also contained information on the acquisition time. At this stage it was possible for the observers to discard images that contained mixed cloud types, middle or high clouds, and cloudless conditions. Only Cu and Sc clouds were selected for analysis, encompassing the entire cloud cover range from 0.1 to total overcast $C = 1$, where C is the decimal fraction of the sky covered by clouds. A total of 2506 episodes with simultaneous cloud cover and irradiance data were available for analysis. As an approximation of the uncertainty of this cloud sky camera, we have taken an average uncertainty of 0.05 for all cloud cover estimation less than 1. A more detailed description is provided in *Serrano et al*. [2014].

Additional data collected consisted in a daily average value of the Ångström parameters α (Ångström exponent) and β (Ångström turbidity coefficient) and the aerosol asymmetry factor, all obtained from the CE-318 Sun photometer located at the field site [*Estellés et al*., 2007].

2.2. LibRadtran Model

CMF_{UVER} estimation requires a cloudless irradiance for every single measurement of UVER. To obtain these data, the UVSPEC module in LibRadtran version 1.7 [*Mayer and Kylling*, 2005] was used. Input variables

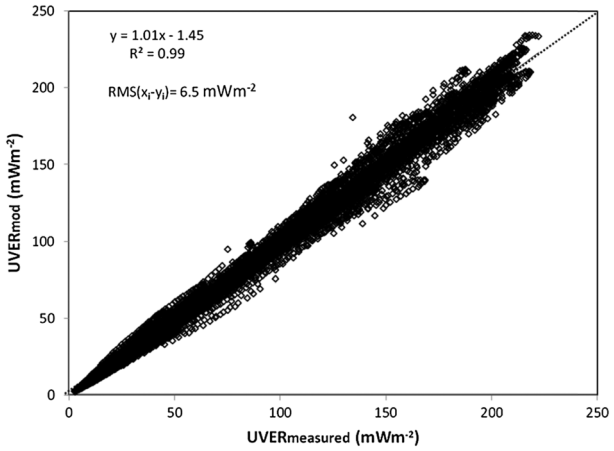

Figure 1. Comparison of modeled UVER irradiance against measured for cloudless skies.

consisted in a midlatitude summer atmosphere, with a 1 nm Atlas plus MODTRAN (moderate resolution atmospheric transmission model) solar spectrum, delta-*m* scaling with discrete ordinates radiative transfer model for a multi-layered plane-parallel medium, and six-stream option. Background stratospheric aerosol conditions were used [*Shettle*, 1989]. Ångström coefficients from the CE-318 Sun photometer were used to parameterize the wavelength dependence of aerosol optical depth. These were based on daily average estimates or interpolated from cloudless episodes. The coefficients were used to scale the default aerosol profile of the UVSPEC program. Several authors have used Ångström α and β coefficients extrapolated to the UVER region to arrive at an aerosol optical depth for UVER (τ_{aer}). Radiative model results compared very well with direct Sun observations from Brewer MkIII instruments [*Kazadzis et al*., 2010; *Nikitidou et al*., 2013] with a typical uncertainty in aerosol optical depth of ±0.02. Therefore, we have also adopted this scheme to estimate (τ_{aer}) for the UVER.

The aerosol asymmetry factor was set to 0.68 which was based on an average figure from the 440 nm channel of the CIMEL instrument. Aerosol single-scattering albedo (ω_{aer}) may be estimated using CIMEL Sun photometer-derived ω_{aer} at 440 nm but not in the UVER band of interest to this study. It may be estimated as a residual term using a radiative model such as LibRadtran [*Goering et al*., 2005; *Petters et al*., 2003]. Residual calculations gave values that varied from 0.60 to 0.80 with a mean around 0.70. However, the technique becomes unusable at high zenith angles due to errors in the estimation [*Bais et al*., 2005; *Serrano et al*., 2014], and in addition, cloud cover prevented retrieval of this data in cloudy days. As an alternative we have used a single value of 0.70 published by *Shettle and Fenn* [1979] and applicable for urban aerosols at wavelengths of 310 nm in the central UVER region. There are slight variations in ω_{aer} with relative humidity which result in changes of ±10% in the monthly average estimates of ω_{aer} from the above figure of 0.70. Given the considerable variability in diurnal relative humidity, the inherent uncertainty in this estimate, and the large magnitudes of cloud depletion expected, a constant value of 0.70 was used.

A UV surface albedo of 0.04 was used also based on the work described in *Serrano et al*. [2014]. All model spectral output was convolved by the Commission Internationale d'Éclairage response curve [*Commission Internationale d'Éclairage*, 1998] which resulted in a UVER data set that was directly comparable to that measured with cloudless conditions. Total column ozone was obtained from daily passes of the Ozone Monitoring Instrument (OMI) on board NASA's Aura satellite (http://ozoneaq.gsfc.nasa.gov). Based on previous studies [*McPeters et al*., 2008; *Antón et al*., 2009] which have compared OMI-Total Ozone Mapping Spectrometer column ozone with surface-based observations, an uncertainty of ±2.2% was used for the column ozone in our model estimates.

Figure 1 shows the LibRadtran model performance for cloudless skies in Valencia by comparing measured data against modeled irradiance. The relationship shows a high coefficient of determination, at 0.99, and an RMS difference of 6.5 mW m^{-2}.

2.3. Monte Carlo Model

The ray tracing Monte Carlo radiative transfer model (MCRTM) was used and is described in *Iwabuchi* [2006]. There are numerous 3-D models in the published literature that have examined radiative processes in inhomogeneous media. Among the most widely used are the Monte Carlo community model of 3-D radiative transfer (I3RC) available at http://i3rc.gsfc.nasa.gov and the Monte Carlo code for the physically correct tracing of photons in cloudy atmospheres available at http://www.bmayer.de/index.html?mystic.html&1. They have been used in a wide range of applications which include modeling satellite-derived properties

of inhomogeneous broken clouds [*Marshak et al*., 2006; *Kokhanovsky et al*., 2007a, 2007b] and aerosol characteristics in the vicinity of broken clouds [*Varnai et al*., 2013]. Other 3-D models which are not ray tracing such as Spherical Harmonics Discreet Ordinate Method are also used to estimate how nadir reflectance changes in broken cloud conditions [*Loeb et al*., 1997]. In our application we have used the ray tracing MCARaTS (Monte Carlo radiative transfer simulator) or MCRTM (Monte Carlo radiative transfer model) as described in *Iwabuchi* [2006] due to its simple yet elegant input structure, its economical use of storage space in describing the model atmosphere, and the software available to process and display the resultant data.

The MCRTM is meant to run mainly in a monochromatic mode, which is a limitation as our erythemal measurements represent UV irradiance convolved by the erythemal response curve which extends from 280 nm to 400 nm [*Diffey*, 2002]. To replicate the UVER measurements with the MCRTM code is too time consuming and impractical, and instead, we select a monochromatic wavelength which is close to the peak in the product of irradiance with the erythemal curve, at 310 nm. Therefore, comparisons with measured and modeled enhancement are not exactly equivalent, and this limitation will appear later in the analysis, when discussing dependence of enhancement on solar zenith angle.

The user defines a three-dimensional domain with length x, y, z, cell size (δx, δy, δz), total number of photons used, and other input parameters to be described later. Initially, each photon is randomly distributed along the top of the domain but with specified zenith angle, a photon weight of one and information on the order of collision, a value above which the photon is considered to be "extinguished" from collisions with aerosols containing a single-scattering albedo less than one. A random number between 0 and 1 is generated, and this establishes the optical path length to the next collision point, allowing then the calculation of the extinction along the path length. The type of collision is established by a random number that samples according to the fraction of scattering coefficients which make up the local scattering cell (air, aerosols, cloud particles, etc.). After collision the photon weight is reduced by a certain amount depending on the extinction path length and single-scattering albedo of the scattering medium. For small photon weights ($<<1$) the Russian roulette method is used [*Kawrakow and Rogers*, 2001] as means of saving computing time. After adjustment for photon weight, new scattering angles are established using a random number which chooses a particular value in a cumulative probability distribution curve.

At each surface cell the above ray tracing method provides total photon counts for photons that have undergone changes in direction and photon weight (diffuse irradiance) and photons that have undergone changes in weight but not direction (direct irradiance). Note that this definition of direct irradiance will include photons that have undergone initial scattering but are scattered back into the viewing cone within which photons are labeled as direct radiation. Furthermore, the program allows the user to choose the cone aperture according to their requirements.

Photons that reach the lateral boundaries of the domain will appear as entering the domain on the opposite side with undisturbed photon count and orientation. This "cyclic" feature ensures that the horizontal domain extends beyond the horizontal constraints of the box, ensuring a full sky coverage but with cyclic cloud features.

Model composition is supplied in the form of two different formats. There is the background atmosphere, assumed to be horizontally homogeneous and composed of a number of layers in which Rayleigh scattering and absorption by ozone and other gases dominate. There is also an inhomogeneous layer, composed of clouds and/or aerosols but which also includes components from the background atmosphere. Scattering within this inhomogeneous layer is performed as discussed above.

In our application we have used a domain of $60 \times 60 \times 28$ cells, each of dimensions $50\,\text{m} \times 50\,\text{m} \times 500\,\text{m}$ (Figure 2). Background conditions consist of 28 atmosphere levels extending from the surface to the top of the atmosphere and are characterized by Rayleigh scattering and absorption by ozone and NO_2. Molecular composition is taken from the Air Force Geophysics Laboratory midlatitude summer atmosphere [*Anderson et al*., 1986] with the ozone profile scaled to (306 ± 17) Dobson unit corresponding to a daily summer average (1 June to 31 August) for the Burjassot region of Valencia. Scattering and absorption cross sections for a wavelength of 310 nm were used in the model. Temperature-corrected ozone was taken from *Molina and Molina* [1986] and NO_2 cross sections from *Vandaele et al*. [2003]. An aerosol concentration profile from *Shettle and Fenn* [1979] was used corresponding to background conditions with 10 km visibility. These were

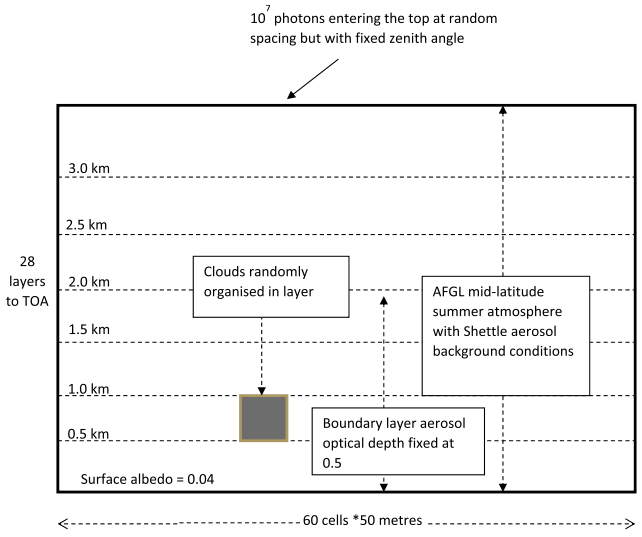

Figure 2. Schematic of the Monte Carlo radiative transfer model. The study area consists of a box of 60 × 60 surface cells of dimensions 50 m × 50 m and 28 layers of 500 m thickness extending to the top of the atmosphere. Scattering and absorption properties are made horizontally homogeneous and for a wavelength of 310 nm. A cloud layer is defined in the second or third layer. Horizontal spacing for clouds varies randomly subject to cloud cover and a user-defined cloud size. Cyclic boundary conditions are used in the horizontal so that a photon leaving one boundary is reflected and appears in the opposite boundary.

further scaled to yield a total column aerosol optical depth for 310 nm of 0.5 representing typical summer conditions in Valencia which are characterized by a relatively high aerosol load [*Serrano et al*., 2014]. Typical aerosol asymmetry parameter and single-scattering albedo of 0.68 and 0.7 were used respectively for all model runs as in the LibRadtran model.

The inhomogeneous layer consisted only of plane-parallel and homogeneous liquid water clouds. A base height of 0.5 km was mostly used, although sensitivity tests extended to base heights of 1.0 and 1.5 km above the surface. Sensitivity to cloud thickness used a constant cloud base of 500 m and with thickness of 100 m, 500 m, and 1000 m. It was necessary to define an additional model level at 600 m for the case of the 100 m cloud. A single-scattering albedo of the cloud medium was taken as 1 (but note that there is also an aerosol mixture within the cloud defined by background conditions). Values of effective droplet radius and asymmetry parameter of 10 μm and 0.84, respectively, were used which are typical of liquid water clouds [*Hu and Stamnes*, 1993]. Cloud optical depth was varied by increasing or decreasing the liquid water extinction efficiency.

Cloud cover was obtained by first organizing clouds in contiguous units or "cloud patches" of 0.5 km in depth and either 1 × 1, 2 × 2, 4 × 4, or 6 × 6 cells in the horizontal. Therefore, for each of these cases the unit cloud would have dimensions of 50 m × 50 m × 500 m, 100 m × 100 m × 500 m, 200 m × 200 m × 500 m, and 300 m × 300 m × 500 m. These cloud patches were then added randomly in the horizontal domain until the desired horizontal cloud cover was reached.

A test was performed initially to determine the standard deviation in model output as a function of photon number. Cloudless conditions were chosen which in theory should give similar irradiance in all surface cells, and any deviation would represent model errors. The model was executed for a 0° zenith angle and, as previously mentioned, for scattering and absorption conditions of 310 nm and nominal extraterrestrial intensity of 542.91 mW nm^{-1} corresponding to the Atlas plus MODTRAN extraterrestrial spectrum [*Thuillier et al*., 2003] integrated over a ±0.5 nm intervals around 310 nm. In actual fact, any value will suffice as only relative values at the surface are of interest. The standard deviation of irradiance from all cells, as percentage of the mean, decreases with photon count, from 8.6% at 10^6 photons to 0.8% at 5 10^7 counts. As a compromise between accuracy and computing time, a photon count of 10^7 was used in all calculations, producing an error of just under 3%. Table 1 shows all conditions that were sampled.

Table 1. Conditions That Were Used to Examine the Enhancement Sensitivity

	Sensitivity to…	Cloud Cover	Cloud Unit Size	Cloud Base Height (m)	Cloud Optical Depth	Cloud Thickness (m)	Solar Zenith Angle (deg)
A	cloud cover	0.1, 0.3, 0.5, 0.7	1 × 1, 2 × 2, 4 × 4, 6 × 6	500	10	500	30
B	cloud base height	0.1 to 0.9 (step 0.1)	1 × 1, 2 × 2, 4 × 4, 6 × 6	500, 1000, 1500	10	500	30
C	cloud optical depth	0.1, 0.3, 0.5, 0.7	4 × 4	500	1, 2, 5, 7, 10, 13, 15, 20	500	30
D	cloud thickness	0.1, 0.3, 0.5, 0.7	4 × 4	500	1, 15	100, 500, 1000, 1500	30
E	solar zenith angle	0.1, 0.3, 0.5, 0.7	4 × 4	500	1, 15	500	0, 15, 30, 45, 60

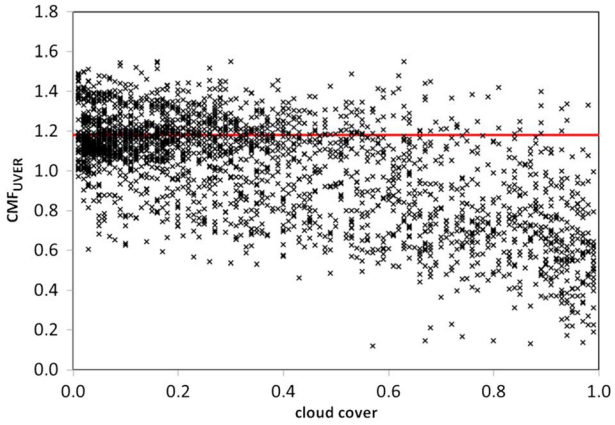

Figure 3. CMF_{UVER} versus cloud cover for all data collected in 2011. A total of 2506 episodes are considered here with only cumuliform-type clouds. The red line represents a level of 1.18, above which there is a 95% level of probability that the ratios are above 1.

2.4. Enhancement and Frequency of Enhancement

In the published literature enhancement (ENH) is usually defined as the percentage increase in surface irradiance above a cloudless value with otherwise the same set of atmospheric input conditions (solar zenith angle, ozone column, etc.). In this study we have chosen to define the frequency of enhancement (FE) over the study region which in the case of the MCRTM is a domain of 60×60 pixels. Using these terms, enhancement and frequency of enhancement may be defined as

$$ENH_{310} = (CMF_{310} - 1)100 \quad (1)$$

$$FE_{310} = \frac{\sum_{i=1}^{60}\sum_{j=1}^{60} e(i,j)}{3600} \quad \text{where} \begin{cases} e(i,j) = 1 \text{ if } CMF_{310}(i,j) > 1 \\ e(i,j) = 0 \text{ if } CMF_{310}(i,j) \le 1 \end{cases} \quad (2)$$

where CMF_{310} (i, j) is the cloud modification factor (ratio of actual to cloudless irradiance) estimated by the MCRTM at 310 nm and for pixel i, j.

Comparison of FE_{310} between measurement and model is not straightforward for various reasons. First, erythemal sensors measure UV irradiance convolved by the erythemal curve and there may be spectral changes with changing environmental conditions. Second, unlike the MCRTM estimates, UVER measurements are not spatially averaged but instantaneous. Assuming a "frozen turbulence" hypothesis in the radiation field, we can equate a spatial average to a temporal average which may be approximated by averaging over similar episodes (i.e., cloud cover). To differentiate between the two estimates, FE_{310} and FE_{UVER} are used, denoting a spatial average from the MCRTM and a temporal average obtained from the UVER measurements, respectively.

In a later analysis, cloud size distribution will be shown to be an important factor which influences FE_{310}. Typical size distributions which vary with cloud cover were obtained by obtaining a size spectrum from a cloudy Landsat scene for the region and incorporating this information in a two-dimensional inverse Fourier transform model (IFTM). The IFTM provided realistic cloud size distributions which varied with cloud cover. Applying the MCRTM to these different cloud size distributions provided the FE_{310}.

3. Results

3.1. Sensitivity of CMF_{UVER} to Cloud Cover From Measurements

Figure 3 is a plot of instantaneous CMF_{UVER} data versus cumuliform-type cloud cover collected for all of 2011. In total, there were 2506 data points that met this condition. As may be noticed, there were a substantial

Table 2. Statistics for Instantaneous CMF_{UVER} Presented at 0.1 Cloud Cover Intervals

Cloud Cover	Average	Standard Deviation	Absolute Maximum	n	Average of Enhancements With CMF > 1.18	FE_{UVER} (%)
0.0–0.09	1.16	0.14	1.54	620	1.31	36.6
0.10–0.19	1.14	0.16	1.54	383	1.28	41.1
0.20–0.29	1.17	0.19	1.51	303	1.28	42.0
0.30–0.39	1.05	0.20	1.54	227	1.26	29.4
0.40–0.49	1.00	0.23	1.42	171	1.26	25.3
0.50–0.59	0.97	0.25	1.48	158	1.26	23.9
0.60–0.69	0.88	0.25	1.54	160	1.32	11.3
0.70–0.79	0.78	0.25	1.38	129	1.26	8.5
0.80–0.89	0.76	0.25	1.41	148	1.27	6.1
0.90–0.99	0.63	0.24	1.33	207	1.28	2.4

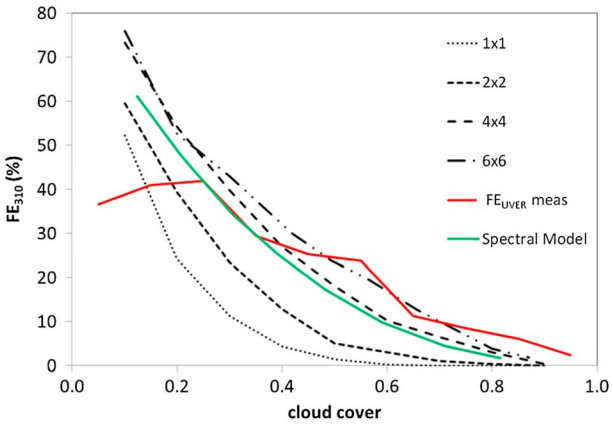

Figure 4. Variability of model frequency of enhancement at 310 nm as a function of cloud cover and cloud cube size, with each cube consisting of horizontal dimensions of 1×1, 2×2, 4×4, and 6×6 cells, each cell measuring 50 m × 50 m in the horizontal and 500 m in depth. Also shown in red are measured FE_{UVER} which are averaged over 0.1 cloud cover intervals (0.0–0.1, 0.1–0.2, 0.2–0.3, …) and FE_{310} using a cloud size distribution model with the MCRTM (in green).

number of ratios exceeding 1, but to arrive at a reliable estimate of enhancement, the uncertainties in the ratios must be taken into consideration. An efficient way of estimating this quantity is to examine errors associated with this ratio in cloudless conditions as this cloud type (or lack of) is easily distinguished with the sky camera [*Sabburg and Calbó*, 2009]. These errors correspond to the RMS estimate of 9.4% in the CMF_{UVER}. By definition, all CMF_{UVER} should be 1 and any departure from this value would be an error. Assuming a totally random distribution, a 95% level of confidence that the CMF_{UVER} is above 1 will be reached at a level of 1.18, shown as a horizontal red line in Figure 3. In total, approximately 30% of observations met this condition of $CMF_{UVER} > 1.18$, although the distribution is strongly skewed toward low cloud cover.

Table 2 presents relevant statistics of the distribution at 0.1 intervals of cloud cover. There is a strong dependence of FE_{UVER} with cloud cover, with maximum enhancement in the interval 0.20 to 0.29 (42% of the total cases in the interval) and decreasing to a minimum of 2% in the near overcast situation (0.90–0.99 cloud cover). A similar decreasing pattern with cloud cover is obtained in the interval average, second column in Table 2. A regression fit to the CMF_{UVER} enhancement (i.e., only for $CMF_{UVER} > 1.18$) gave the following relationships:

$$\begin{aligned} FE_{UVER} &= 16.4C^2 - 71.0C + 54.1 \\ R^2 &= 0.95;\ \ \mathrm{RMS}(x_i - y_i) = 4.6\%;\ n = 10 \end{aligned} \tag{3}$$

Equation (3) is the frequency of enhancement (FE_{UVER}) averaged every 0.1 cloud cover interval. Best fit is obtained with a second degree polynomial in C.

3.2. Monte Carlo Simulation of Sensitivity to Cloud Cover

The MCRT model was executed for the input variables shown in Table 1, row A, which encompass four different cloud cover, four different patch areas but constant thickness, base height, and optical depth (Figure 4). There is a strong dependence on cloud cover and packet dimensions. Frequency of enhancement is greater than 50% for fractional cloud cover of 0.1 and increases as the packet size becomes larger. As cloud cover increases, the frequency of enhancement drops rapidly for all packet areas. Greatest and lowest sensitivity to cloud cover occurs with the 1×1 and 6×6 packets, respectively.

To test the model uncertainty, four sets of cloud cover conditions were chosen ($C = 0.1$, 0.3, 0.5, and 0.7), each with constant cloud optical depth, thickness, base height, and patch area which were 10, 500 m, 500 m, and 4×4, respectively. The simulations were repeated 10 times for each condition with 10^7 photons as mentioned in the previous section. What is being tested here is the uncertainty in the frequency of enhancement

Table 3. Uncertainty in Model Frequency of Enhancement at 310 nm for Cloud Cover Scenarios of 0.1, 0.3, 0.5, and 0.7[a]

Cloud Cover	Average Enhancement (%)	Standard Deviation (%)	Error (Standard Deviation/Average) (%)	*n*
0.1	73.4	0.3	0.5	10
0.3	41.3	0.7	1.6	10
0.5	17.6	1.2	7.0	10
0.7	7.2	0.6	8.9	10

[a]A cloud base of 500 m, cloud thickness 500 m, and optical depth of 10.0 were used. Calculations were repeated 10 times to arrive at the statistic.

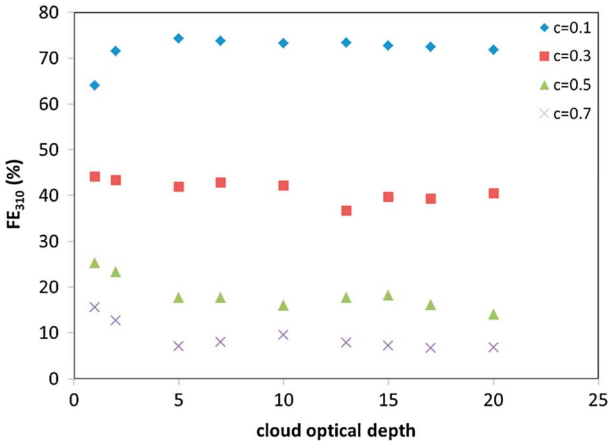

Figure 5. Variability model of frequency of enhancement at 310 nm as a function of cloud optical depth for four intervals of cloud cover fraction: 0.1, 0.3, 0.5, and 0.7.

calculation FE_{310} related to the random cloud arrangement which is being used for all estimates. Table 3 shows the result of the simulation which gave standard deviations in the frequency of enhancement of 0.3%, 0.7%, 1.2%, and 0.6% for cloud cover 0.1, 0.3, 0.5, and 0.7, respectively. We have chosen the highest standard deviation of 1.2% as being representative of the inherent uncertainty in the MCRT estimates.

3.3. Monte Carlo Simulation of Sensitivity to Cloud Base Height

The MCRTM was executed for a constant cloud thickness (500 m) and optical depth (10), three cloud base heights (500 m, 1000 m, and 1500 m), and varying cloud cover and cloud size (Table 1). There is a general trend of decreasing FE_{310} with increasing base height, but the change is not large and confined to less than 6.4%. Considering that the uncertainty in estimation has been taken to be 1.2%, only 12 out of the 72 cases considered above are larger than twice the standard deviation of 1.2%. We conclude that FE_{310} is only weakly sensitive to cloud base height.

3.4. Monte Carlo Simulation of Sensitivity to Cloud Optical Depth

In this section cloud base height and thickness are set constant at 500 m and sensitivity to cloud optical depth is examined for cloud cover fractions of 0.1, 0.3, 0.5, and 0.7, Figure 5. For a specific cloud fraction, there is decreasing FE_{310} with cloud optical depth. The trends are all significant at the 95% level of confidence. However, the dependence on optical depth is weaker than the cloud cover dependence. For example, at cloud cover 0.5, the enhancement due to the full range of optical depth extends from 25% to 14%. Similar characteristics appear in the relationships for the other cloud cover fractions.

3.5. Monte Carlo Simulation of Sensitivity to Cloud Thickness

The sensitivity of enhancement to cloud thickness is shown in Figure 6. For display purposes four cloud fractions are presented, 0.1, 0.3, 0.5, and 0.7, along with two extreme cloud optical depth, 1 and 15.

There is a strong decrease in frequency of enhancement as cloud thickness grows from 100 m to 1500 m. Highest enhancement occurs at a cloud cover of 0.1 and decreases with increasing cloud cover. In all cases the frequency of enhancement versus cloud thickness trend is nonlinear. As shown in Figure 6, cloud optical depth affects FE_{310}, but to a much smaller extent than cloud thickness or cloud cover, with typical decreases in FE_{310} of 8–9% for changes in optical depth from 1 to 15.

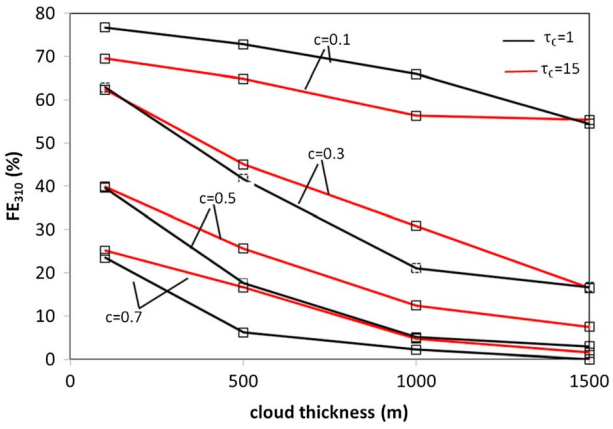

Figure 6. Variability of model frequency of enhancement at 310 nm with cloud thickness for four cloud cover episodes (0.1, 0.3, 0.5, and 0.7) and cloud optical depth of 1 and 15.

3.6. Monte Carlo Simulation of Sensitivity to Solar Zenith Angle

As in the previous figure, four cloud cover episodes ($C = 0.1$, 0.3, 0.5, and 0.7) and two cloud optical depths 1 and 15 are shown in Figure 7. There is a strong dependence of FE_{310} on solar zenith angle for all cloud cover episodes. Estimated FE_{310} data group into cloud fraction but show little dependence on cloud optical depth. For a given

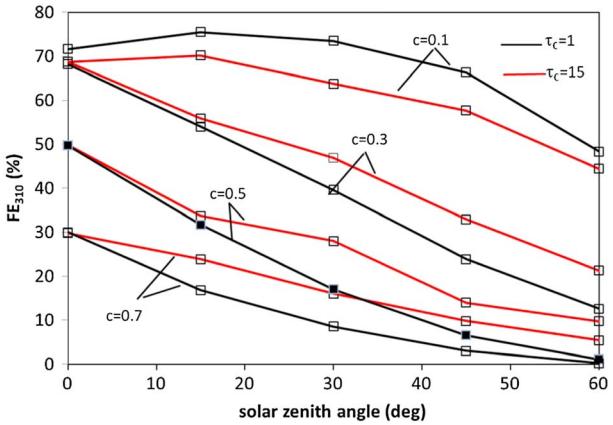

Figure 7. Variability of model frequency of enhancement at 310 nm with solar zenith angle for four cloud cover episodes (0.1, 0.3, 0.5, and 0.7) and cloud optical depth of 1 and 15.

solar zenith angle and cloud fraction, the variability induced by cloud optical depth is less than twice the standard error of the Monte Carlo simulation at 10^7 photons (<2.4%). By contrast, there is no significant trend in observational results in CMF_{UVER} when plotted versus solar zenith angle, Figure 8. However, as pointed out earlier, the two estimates are not equivalent as FE_{310} represents a monochromatic estimate at 310 nm while FE_{UVER} is an integrated measurement of spectral irradiance with the erythemal curve.

Solar zenith angle changes impact on spectral composition of UVER, with a shift toward higher wavelengths and higher transmission as zenith angles decreases [*Kylling et al*., 1997]. Diagnostic tests with LibRadtran 1.7 with overcast clouds of optical depth 10 (not shown) reveal typical increases in CMF_{UVER} of 17% with solar zenith angle from 0 to 70°. Opposing this trend is a decrease in UVER as a result of blocking. These two opposing trends to a large extent cancel out, showing only a weak sensitivity to zenith angle in FE_{UVER}. By contrast, FE_{310} from the MCRTM decreases with zenith angle as there are no spectral changes.

3.7. Physical Mechanisms in the Enhancement Process

Considering a homogeneous infinite cloud with (or without) a constant optical depth, it is evident that the irradiance received at the surface will never exceed the incoming irradiance at the cloud top as there will always be some reflection from the cloud layer which will depend on the optical depth. An enhancement of surface irradiance above a cloudless value must be related to edge effects induced by cloud gaps. It might involve a scattering of some radiation from a cloud edge into the viewing cone of the direct radiation, leading to enhancement of direct radiation but most importantly to enhanced diffuse radiation above a cloudless value. Within this context, the blocking of downward traveling radiation by the cloud geometry is crucial to the enhancement.

Figure 9 illustrates the nature of the blocking. Consider two cloud cubes separated by distance D and dimensions $L \times L \times H$. Downward traveling radiance from point P will be affected by surface δA in the adjacent block. This effect may be expressed as a view factor (VF) for a vertical surface in point P; a totally obstructed environment will have a view factor of 1, and no obstruction will have a VF of 0 [*Steyn*, 1980]. Furthermore, the VF is a function of the cloud distance, D, and geometry, H and L. Exporting this context to the MCRTM model is difficult as the cloud cubes and the resultant enhancement have been distributed randomly in the horizontal. However, a crude approach may be followed to illustrate the importance of this blocking mechanism. For a particular calculated cloud cover and cloud size we have changed the cube arrangement into a regular array over the entire domain, essentially in a similar fashion to Figure 9. For low cloud cover ($C = 0.1$) of small horizontal dimensions (1×1) there will be many cubes distributed in large numbers throughout the

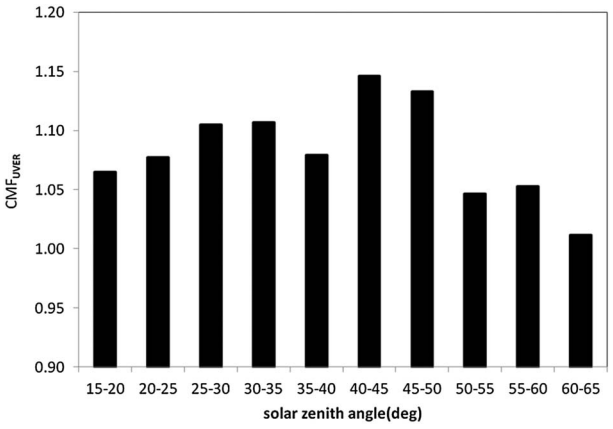

Figure 8. Plot of measured CMF_{UVER} versus solar zenith angle. Ratios have been estimated over 5° zenith angle range. All cloud cover data used in the study have been included.

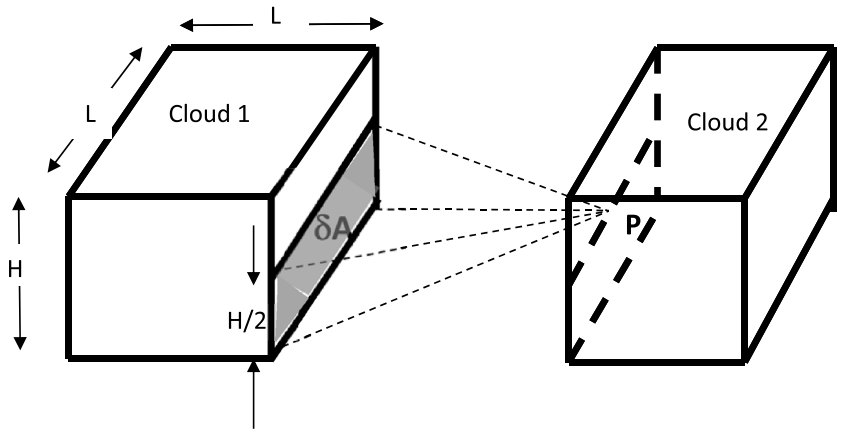

Figure 9. Cloud geometry showing the view factor for element of cloud δA as seen by a point P in the center of a vertical facet of cloud 2. The view factor will determine how much radiance from P will reach the ground. Each cube has dimensions $L \times L \times H$ and is separated by distance D.

model domain, so that the distance D will be small (~132 m). By contrast, if $C = 0.1$ and the array is large (6×6), there will be only a few cloud cubes with a large distance of separation D (~300 m).

Applying the relevant estimates of D, H, and L to $C = 0.1$ and the two horizontal dimensions with $H = 500$ m, view factors of 1.49% and 36.7% are obtained for the 6×6 and 1×1 arrays, respectively. Therefore, the blocking mechanism is much more efficient with small cloud size for constant cloud cover and cloud thickness. Other factors are of course important. Increasing cloud thickness will increase the VF and increase the amount of blocking, while increasing solar zenith angle will decrease the irradiance received by the vertical facets of the cubes. As enhancement is related to "leakage" by the vertical facets of the cube, cloud optical depth plays a relatively small part in the process, although it is very important in affecting the spatial average of incoming surface irradiance.

4. Comparison of Frequency of Enhancement Data From Model and Measurements

It is evident from Figure 4 that FE_{UVER} data show a pronounced dependence on cloud cover, from a maximum of around 40% for $c \sim 0.2$ to just a few percent at c equal to 0.9. Model estimates of FE_{310} show monotonic decreases with cloud cover and increases with cloud patch size, but no overall agreement with measurements. From the previous analysis we can discount these differences to be due to cloud optical depth, cloud base height, and cloud zenith angle, while our cloud thicknesses of 500 m are in agreement with observations in other studies for low-level Sc clouds [*Chakrapani et al*., 2002; *Minnis et al*., 1992] and close to an average figure of 400 m given for a midlatitude atmosphere [*Wood*, 2012]. Discounting these factors, cloud coverage and cloud size are the two outstanding factors that influence FE_{310}. It is well known that clouds are not homogeneous in their horizontal structure but exhibit a spectrum of values for liquid water, optical depth, and spatial dimensions [*Cahalan and Joseph*, 1989; *Cahalan et al*., 1994; *Boers*, 1997; *Boers et al*., 2000; *Koren et al*., 2008]. Our next procedure is to develop a more realistic cloud size distribution.

A Landsat thematic mapper (TM) image collected on 7 August was selected for the region (Appendix A) containing Cu and Sc clouds. A total of 53 linear transects were selected crossing various cloud scenes, enabling separation of cloudy from clear pixels by the relatively high reflectance for clouds as opposed to land surfaces. These transects vary in size from 170 pixels (5100 m) to 615 pixels (18450 m). Each reflectance transect was transformed into frequency space using the fast Fourier transform algorithm of Interactive Data Language (IDL) and subsequently turned into a power spectrum, which on average gave a power slope of −2.4. Knowing the power spectrum, an inverse fast Fourier transform (IFFT) algorithm was used to create 60×60 two-dimensional scenes in real space which contained the power spectrum. This spatial field is a pseudoreflectance since the spatial average is zero, but the variance is in agreement with the slope of the power spectrum. Therefore, $S(i, j)$ has the original power spectrum and a property that

$$\sum_{i=1}^{60} \sum_{j=1}^{60} S(i,j) = 0.0 \tag{4}$$

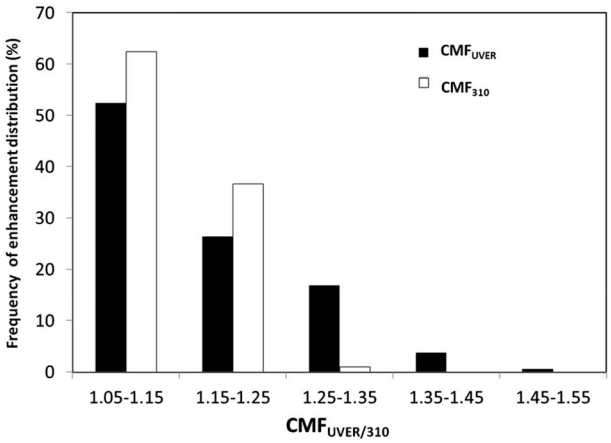

Figure 10. Frequency of enhancement distribution showing CMF_{UVER} and CMF_{310} data.

Cells with negative estimates are set to zero, and cloud cover is estimated by adding all nonzero cells, setting this value to 1 and dividing by the total cells in the field, 3600. By adding (or subtracting) a constant value to $S(i, j)$, cloud cover may be changed, each resulting in a different spectrum of cloud sizes. The final step involves setting a constant cloud optical depth of 10 to all cloud cells. This procedure was followed 10 times for each cloud cover interval and used as model input into the MCRTM. Results are presented in Figure 4 under Spectral Model.

Agreement between the two data sets, FE_{UVER} and FE_{310} (spectral), has improved compared to the model output with fixed cloud dimensions, Figure 4. At fractional cloud covers greater than 0.2, the two data sets are in broad agreement, with an average FE_{UVER} for all measurements of 23% compared to 25% for the FE_{310} (spectral). A marked disagreement between measurement and modeling is noted at fractional cloud cover of less than 0.2 as measurements show a slight decline but model estimates give increasing enhancement. We attribute this difference to the neglect of cloud areas smaller than 1×1 cells (50 m × 50 m).

The cloud areas which were fed into the MCRTM had a power slope of −2.4, and this procedure is in accordance with *Koren et al*. [2008] who used Landsat TM data to observe that areas of cumulus clouds in many regions of the world obeyed a power law distribution, with a high number of small clouds and a smaller number of large clouds.

Examining the FE_{310} output in Figure 4, FE_{310} decreases with cloud area, with cells of dimension 1×1 (50 m × 50 m) being the lowest considered in the model. *Wielicki and Welch* [1986], *Cahalan and Joseph* [1989], and *Koren et al*. [2008] conclude that smaller subpixel clouds have a large influence on scene reflectance which our analysis, being limited to a 50 m cells in the MCRTM field, is likely to have missed. Therefore, it is likely that neglect of the very small cloud areas, which lower the enhancement, will induce the erroneously high spectral FE_{310} obtained with the MCRTM.

As a further assessment of the model performance, a histogram of enhancement values is calculated for all measured data and compared with MCRTM estimates, Figure 10. Measurements of CMF_{UVER} that were above 1 were grouped and summed in intervals covering the range 1.05 to 1.55 with increments of 0.1. The IFFT model was executed 10 times with constants adjusted to give regional cloud cover of 0.13, 0.21, 0.32, 0.41, 0.47, 0.59, 0.71, and 0.81. Each of the 10 model output scenes with their specific cloud distribution and cloud optical depth of 10 was processed by the MCRTM, and all CMF_{310} estimates greater than 1 were grouped together into the range intervals listed above. This involved 1007 measurements and 6812 data points for the model. Figure 10 presents the results of the comparison.

Highest frequency of CMF_{UVER} value, greater than 50% in both CMF_{UVER} and CMF_{310}, is obtained in the range between 1.05 and 1.15. As the CMF_{UVER} value increases, the frequency drops: 26% (CMF_{UVER}) and 37% (CMF_{310}) in the interval 1.15 to 1.25 and 17% (CMF_{UVER}) and 1% (CMF_{310}) in the interval 1.25 to 1.35. The MCRTM gives no data beyond an enhancement interval 1.25 to 1.35. A chi-square goodness of fit between the CMF_{UVER} and CMF_{310} distributions in Figure 10 was performed using the null hypothesis that there is no difference between parent distribution (CMF_{UVER}) and the CMF_{310} distribution. Results gave a chi-square coefficient of 25, indicating that there is a probability of less than 0.1% that the difference between the two distributions is due to chance. Therefore, the null hypothesis is rejected, and the differences are real. Furthermore, examining Figure 10, it is evident that differences between the two distributions are large for enhancement factors greater than 1.25, very likely in the region of low cloud cover as shown in Figure 4 where FE_{UVER} and FE from the spectral model diverge.

5. Discussion

One important result presented in the paper is the high frequency of enhancement obtained in both our measurement and the modeling scheme. Examining the published literature, it interesting to note that *Sabburg and Calbó* [2009] in Towoomba, Australia, report FE_{UVER} for cumuliform clouds that vary between 30% and 40% depending on CMF measurements. Their results agree closely with our estimate of a total FE_{UVER} of 30% when all our observations are grouped. *Kuchinke and Núñez* [1999], analyzing 3 years of data for southwest Sweden, report UVER enhancement in 44% and 49% of episodes dominated by cumulus clouds of little vertical extent and strong vertical extent, respectively, with 1 to 3 oktas. In our study the number of episodes of enhancement by cumulus clouds is 41% and 42% with cloud cover of 0.10–0.19 and 0.20–0.29, respectively (Table 2).

Frequency of enhancement decreases strongly with cloud cover, an observation that was also supported by model calculations. In our analysis instantaneous data on enhancement (Figure 4) were grouped into enhancement frequency and these episodes were averaged into cloud cover intervals to produce a trend shown in Figure 4. Most studies dealing with cloud effects on UV document decreasing trend of CMF_{UVER} with increasing cloud cover as reviewed by *Calbó et al*. [2005]. However, studies that explicitly deal with enhancement as a function of cloud cover are much less common. Within this context *Foyo-Moreno et al*. [2003] and *Grant and Heisler* [2000] provided histograms of CMF_{UV} versus fractional cloud cover in the UV ranges 295 nm to 385 nm and 280 nm to 320 nm, respectively. Although no cloud type information was provided, both studies show that on average, CMF_{UV} decreases with cloud cover, which is in rough agreement with our results that both FE_{UVER} and FE_{310} decrease with cloud cover.

An MCRTM approach as used in this study permitted a closer examination of the various processes involved in UV enhancement. Scattering of photons from individual cloud droplets is the principal source term, which may occur by reflection from cloud sides or scattering as the photon travels through the cloud [*Mims and Frederick*, 1994; *Sabburg and Wong*, 2000; *Parisi et al*., 2004, among others]. The basic physical characteristics of the cloudy regions tend to counter this enhancement, trapping some of these scattered photons that could potentially reach the surface. Therefore, in the case of low-level liquid water clouds, the trend is for the enhancement to drop with cloud cover as shown in our Figure 4. However, the geometry of cloud volumes within cloud cover intervals is also important in affecting enhancement and, in particular, cloud spacing and cloud size.

Although there is little sensitivity to cloud base height, there is a strong dependence on cloud thickness. Our Figure 6 shows decreasing frequency of enhancement with clouds changing in depth from 100 m to 1500 m, supporting the argument by *Estupiñán et al*. [1996] that deeper clouds of the cumulus type would enhance more compared to the shallow stratocumulus as a result of side reflection. It is important to note that cloud optical depth in Figure 6 has been assigned extreme values, 1 and 15, while cloud thickness has changed. These results along with Figure 6 point to the lower role that cloud optical depth plays in the enhancement process.

Areas of cloud patches making up the cloud environment affect significantly the enhancement process as shown in Figure 4. In the real environment low-level liquid water clouds display a spectrum of cloud sizes in response to forcing by surface convection [*Cahalan and Joseph*, 1989; *Boers*, 1997; *Boers et al*., 2000]. To arrive at a more realistic cloud size distribution, an IFFT algorithm was developed that used a reflectance power spectrum from a Landsat TM image covering the Valencia region and containing regions of cumulus and stratocumulus clouds.

Applying a size distribution into the MCRTM gave more realistic FE_{310} that compared favorably with the measurements. However, the model failed to produce the measured enhancement at very low cloud cover of 0.2 or less, and we attribute this to the limitations imposed by the spatial resolution of 50 m × 50 m of the MCRTM. Clouds become increasingly more efficient reflectors (and poorer transmitters) as their size diminishes [*Koren et al*., 2008] so that failure to account for the subpixel clouds would produce erroneously high model values. Recent published observations [*Petters et al*., 2003; *Twohy et al*., 2009; *Varnai et al*., 2013] document enhanced scattering near cloud "gaps," suggesting complex relationships between the cloud environment and the clear air in its vicinity.

The model produced direct beam enhancement, a feature that appeared in all episodes of enhancement. As part of the MCRTM input, it is possible to specify a cone aperture in degrees such that photons arriving at the surface

Table 4. Model Estimates of Percentage of Cells Which Experienced Direct and Global Irradiance Enhancement[a]

Cloud Cover	Cells With Direct Irradiance Enhancement (%)	Cells With Global Irradiance Enhancement (%)	Cells With Both Global and Direct Irradiance Enhancement (%)
0.13	27.3	63.6	27.3
0.21	17.3	47.6	15.2
0.31	15.7	33.8	15.7
0.41	2.4	24.4	0.1
0.47	3.1	18.0	0.1
0.59	2.8	9.9	0.2
0.72	3.3	5.8	0.1
0.82	3.8	1.4	0.0
0.91	2.6	0.2	0.0

[a]The fourth column represents percentage of cells which experienced both direct and global irradiance enhancement.

and falling inside this cone are labeled as "direct radiation" regardless of the number of previous scattering events. Given the Sun/Earth geometry, a cone aperture of 0.533° defines a departure from parallel radiation [*Iqbal*, 1983], but a cone aperture of 5° is more consistent with recent shadowband assemblies designed to block direct radiation [*McArthur*, 2004]. To illustrate direct beam enhancement, we have run again the MCRTM with a 5° direct beam cone varying cloud cover and base conditions of cloud size (4 × 4), cloud thickness and cloud base height (500 m), and optical depth (10). Table 4 presents the results. There is direct beam enhancement for all cloud cover episodes, although the percentage of cells enhanced is lower than global irradiance enhancement in most cloud episodes. It is interesting to note that in nearly all cases a direct beam enhancement will occur with a global irradiance enhancement (fourth column) when cloud cover is lower than 0.3. These results support the findings of *Sabburg and Wong* [2000], *Parisi et al.* [2004], and *Núñez et al.* [2012] that enhancement is at least partly related to scattering of direct beam radiation by clouds in the circumsolar zone. Typically, it may occur near cloud edges, in narrow cloud gaps or other events with a specific Sun/cloud geometry.

The sensitivity test performed with the MCRTM showed decreasing FE_{UVER} with solar zenith angle, with the relationship being most pronounced at middle to high cloud cover (Figure 7). Although the two data sets are not exactly comparable, no evidence was found in the measurements supporting this process (Figure 8) and the CMF_{UVER} values showed no significant trend with solar zenith angle. As discussed earlier, these differences are likely related to spectral changes occurring in UVER with zenith angle, unlike the MCRTM irradiance which measures at only one wavelength, 310 nm. *Kylling et al.* [1997] discuss this wavelength shift in the incoming UV radiation with solar zenith angle, with a resultant increase in cloud transmission.

6. Conclusions

Cloud cover is largely dominant in determining FE_{310} and FE_{UVER}, reaching a maximum for low cloud amounts (~40% at 0.1 cloud cover) and decreasing with cloud cover to values of under 10% for 0.8 cloud amounts.

The area of cloud patches making up the fractional cloud cover is important in affecting FE_{310}. Lowest enhancement occurs with the smallest patches and vice versa. To obtain realistic results which compare well with measured FE_{UVER} data, there is a need to use a cloud size distribution which varies with cloud cover.

Both increasing cloud thickness and increasing solar zenith angle decrease FE_{310}. However, FE_{UVER} only shows a weak change with increasing solar zenith angle, very likely due to spectral changes in the incoming UVER irradiance which counteract blocking effects.

Compared to the above three processes, cloud optical depth and cloud base height have considerably smaller effect on frequency of enhancement.

Appendix A

We next examine typical cumulus and stratocumulus cloud sizes using Landsat data for the Valencia region. Using the LandsatLook Viewer at the USGS (United States Geological Survey) site (http://landsatlook.usgs.gov), a suitable scene was retrieved. It was taken on 7 August 2014 with Sun elevation 60.67°, center latitude/longitude of 39°57′35″/1°58′22″, respectively, path/row 199/033, and sensor OLI_TIRS. The data form

part of the Operational Landsat Imager of Landsat 8 which provides images in 11 bands, and for our application we chose bands in blue (0.45 μm–0.51 μm), green (0.53 μm–0.59 μm), and red (0.64 μm–0.67 μm), available at 30 m resolution.

The image was displayed in real colour using the IDL image routine, and it was possible to distinguish clearly cumulus and stratocumulus cloud arrays scattered throughout the scene. A total of 28 different regions were selected, and for each region horizontal transects were selected crossing areas of scattered cloud. The blue band was used as a filter to distinguish between cloud and surface areas. As a result, individual pixels in a transect throughout a particular scene would reflect highly with clouds and considerably lower and with low variability if sensing land. A transect, thus, is a convenient way of separating cloud from land and to gauge the size of the cloud portion. A total of 53 transects were taken in the 28 cloud scenes, with transects varying in size from 170 pixels (5100 m) to 615 pixels (18450 m) and with a mean of 335 pixels (10050 m).

Using the discrete Fourier transform routine of IDL, each of the 53 transects was converted into functions of frequency space. For any transect m we can write

$$\mathrm{DFT}(f(t)) = g(k) = \sum_{n=0}^{N-1} f(t_n) e^{-i2\pi kt} \tag{A1}$$

where $f(t_n)$ is reflectance along N discreet points in the transect. In turn k is frequency or wave number defined by $k_i = n_i/T$, T being the length of the series and n_i is a sequence number. Transformation of $g(k)$ into a power series of k, $S(k)$ is readily obtained by taking the complex conjugate of $g(k)$, also available as an IDL routine:

$$S(k) = g(k) x g(k)^* \tag{A2}$$

$$S(k) = C_0 k^{\alpha} \tag{A3}$$

$$\ln(S(k)) = C_0 + \alpha \ln(k) \tag{A4}$$

Lovejoy et al. [2001] postulated that for cloud fields, $S(k)$ has the form of a power function which may be written as in equations (A3) and (A4). Furthermore, the sign and magnitude of the slope of the logarithmic expression (A4) defines how quickly the power $S(k)$ is changing with wave number. Our analysis with the 53 transects gave estimates of a varying between −1.8 and −3.0 with a mean at −2.4. Our interpretation is that power decreases with increasing k, meaning that most of the variance in the time series is concentrated in low wave numbers or large clouds.

We next wish to change this information into two-dimensional cloud scenes where cloud areas obey the power slope of −2.4. It is obtained by first creating a two-dimensional frequency scene in which all transects obey the power slope −2.4 and second taking its inverse Fourier transform to get the equivalent information in two-dimensional space. Denoting k_i and l_j as wave number sequences in k and l space, we can write the two-dimensional frequency scene as

$$\begin{aligned} g(k_i, l_j) &= \left[S\left(\vec{k}\right)\right]^{1/2} e^{-i2\pi\omega\left(k_i, l_j\right)} \\ S\left(\vec{k}\right) &= C\left(k_i^2 + l_j^2\right)^{-\alpha} \end{aligned} \tag{A5}$$

And the phase function component $w(k_i, l_j)$ is allowed to vary randomly between 0 and 1 for any combination of k and l.

The two-dimensional Fourier transform of $g(k_i, l_j)$ provides the information on the spatial field:

$$F(x_m, y_n) = \sum_{k_1}^{k_N} \sum_{l_1}^{l_N} \left[C\left(k_i^2 + l_j^2\right)^{1/2}\right]^{-\alpha} e^{2\pi i w\left(k_i, l_j\right)} e^{2\pi i w\left(k_i x_m, l_j y_n\right)} \tag{A6}$$

where $x_m = \frac{m\delta x}{X}, y_n = \frac{n\delta y}{Y}$ are normalized coordinates in the x and y directions, X and Y are maximum lengths of the x and y scale, and m, n are sequence numbers. In order to generate a real field, the imaginary part of (A6) must vanish, which may be obtained by imposing the following controls on k_i and l [*Press et al*., 2007]. Using T as the total series length and N as the total sequence number, if $w(k, l)$ is defined in the range $0 \le k_i \le N/T$ and $0 \le l_j \le N/T$, then $w(k, l)$ is generated as a random number between 0 and 1 in the range $0 \le k_i + l_j < N/T$. Otherwise, if $k_i + l_j > N/T$, then $w(k, l) = -w(N/T - k_i, N/T - l_j)$.

The spatial field has the same spectral property as the reflectance field, but it is not a true reflectance as the spatial average is zero. However, for our purposes it contains information on the cloud size spectrum which may be obtained by adding a constant term C_0 and imposing the condition that for cell $F(x_m,y_n)$:

$$\begin{aligned} &F(x_m,y_n) \le 0 \quad \text{then} \quad F(x_m,y_n) = \text{Surf}_i(x_m,y_n) \text{representing surface} \\ &F(x_m,y_n) > 0 \quad \text{then} \quad F(x_m,y_n) = CLi(x,y) \text{representing cloud} \\ &CI = \frac{\sum_{i=1}^{M} CL_i}{3600} \end{aligned} \tag{A7}$$

And cloud cover is given by the summation of M cloudy cells.

Acknowledgments

This work was financed jointly by the Spanish Ministry of Economy and Competitiveness and the European Regional Development Fund through projects CGL2011-24290 and CGL2012-33294 and by the Valencia Autonomous Government through project PROMETEUII/2014/058. Núñez was in Valencia thanks to the "Attracting Talent" program by the University of Valencia. The authors would like to thank the USGS ESPA On-Demand System (http://espa.cr.usgs.gov) for processing the Landsat products. The authors are grateful for constructive and useful comments by three referees and specially referee 3. Data for this study may be accessed by writing to the head of the Solar Energy Group, Jose Antonio Martinez-Lozano (jmartine@uv.es). MCARaTS and Libradtran are freely available software.

References

Alados, I., I. Foyo-Moreno, F. J. Olmo, and L. Alados-Arboledas (2000), Estimation of photosynthetically active radiation under cloudy conditions, *Agric. For. Meteorol.*, *102*, 39–50.

Alados-Arboledas, L., I. Alados, I. Foyo-Moreno, F. J. Olmo, and A. Alcántara (2003), The influence of clouds on surface UV erythemal irradiance, *Atmos. Res.*, *66*, 273–290.

Anderson, G. P., S. A. Clough, F. X. Kneizys, J. H. Chetwynd, and E. P. Shettle (1986), AFGL atmospheric constituents profiles, AFGL-TR-86-0.10, 43 pp.

Antón, M., M. Lopez, J. M. Vilaplana, M. Kroon, R. McPeters, M. Banon, and A. Serrano (2009), Validation of OMI-TOMS and OMI-DOAS total ozone column using five Brewer spectroradiometers at the Iberian Peninsula, *J. Geophys. Res.*, *114*, D14307, doi:10.1029/2009JD012003.

Bais, A. F., A. Kazantzidis, D. S. Balis, C. S. Zerefos, and C. Meleti (2005), Deriving an effective aerosol single scattering albedo from spectral surface UV irradiance measurements, *Atmos. Environ.*, *39*, 1093–1102.

Blumthaler, M., W. Ambach, and M. Salzberg (1994), Effects of cloudiness on solar and diffuse UV irradiance in a high-mountain area, *Theor. Appl. Climatol.*, *50*, 23–30.

Bodecker, G. E., and R. L. McKenzie (1996), An algorithm for inferring surface UV irradiance including cloud effects, *J. Appl. Meteorol.*, *35*, 1860–1877.

Boers, R. (1997), Simultaneous retrievals of cloud optical depth and droplet concentration from solar irradiance and microwave liquid water path, *J. Geophys. Res.*, *102*, 29,881–29,891.

Boers, R., A. Van Lammeren, and A. Feijt (2000), Accuracy of cloud optical depth retrievals from ground-based pyranometers, *J. Atmos. Oceanic Technol.*, *17*, 916–927.

Bordewijk, J. A., H. Slaper, H. A. Reinen, and E. Schlamann (1995), Total solar radiation and the influence of clouds and aerosols on the biologically effective UV, *Geophys. Res. Lett.*, *22*, 2151–2154.

Cahalan, R. F., and J. H. Joseph (1989), Fractal statistics of cloud fields, *Mon. Weather Rev.*, *117*, 261–272.

Cahalan, R. F., W. Ridgway, W. J. Wiscombe, S. Golmer, and H. Harshvardan (1994), Independent pixel and Monte Carlo estimates of stratocumulus albedo, *J. Atmos. Sci.*, *54*, 3776–3790.

Calbó, J., D. Pages, and J.-A. González (2005), Empirical studies of cloud effects on UV radiation: A review, *Rev. Geophys.*, *43*, RG2002, doi:10.1029/2004RG000155.

Chakrapani, V., R. Doelling, A. D. Rapp, and P. Minnis (2002), Cloud thickness estimation from GOES-8 data over the ARM-SGP site, in *Twelfth ARM Science Team Meeting Proceedings*, edited by D. Carrothers and W. A. Richland, 7 pp., U.S. Department of Energy, St. Petersburg, Fla.

Commission Internationale d'Éclairage (1998), *CIE S007E-1998: Erythema Reference Action Spectrum and Standard Erythema Dose*, CIE Central Bureau, Vienna, Austria.

Diffey, B. L. (2002), Sources and measurement of ultraviolet radiation, *Methods*, *28*, 4–13.

Estellés, V., J. A. Martínez-Lozano, M. P. Utrillas, and M. Campanelli (2007), Columnar aerosol properties in Valencia (Spain) by ground-based Sun photometry, *J. Geophys. Res.*, *112*, D11201, doi:10.1029/2006JD008167.

Esteve, A. R., M. J. Marín, F. Tena, M. P. Utrillas, and J. A. Martínez-Lozano (2010), The influence of cloudiness over the values of UVER in Valencia, Spain, *Int. J. Climatol.*, *30*, 127–136, doi:10.1002/joc.1883.

Estupiñán, J. G., S. Raman, G. H. Crescenti, J. J. Streicher, and W. F. Barnard (1996), Effects of clouds and haze on UV-B radiation, *J. Geophys. Res.*, *101*, 18,607–16,816.

Foyo-Moreno, I., I. Alados, F. J. Olmo, and L. Alados-Arboledas (2003), The influence of cloudiness on global UV irradiance, *Agric. For. Meteorol.*, *120*, 101–111.

Goering, C. D., T. S. L'Ecuyer, G. L. Stephens, J. R. Slusser, G. Scott, J. Davis, J. C. Barnard, and S. Madronich (2005), Simultaneous retrievals of column ozone and aerosol optical properties from direct and diffuse solar ultraviolet irradiance measurements, *J. Geophys. Res.*, *110*, D05204, doi:10.1029/2004JD005330.

Grant, R. H., and G. M. Heisler (2000), Estimation of ultraviolet-B irradiance under variable cloud conditions, *J. Appl. Meteorol.*, *39*, 904–916.

Holben, B. N., et al. (1998), AERONET—A federated instrument network and data archive for aerosol characterization, *Remote Sens. Environ.*, *66*, 1–16.

Hu, Y. X., and K. Stamnes (1993), An accurate parameterization of the radiative properties of water clouds suitable for use in climate models, *J. Clim.*, *6*, 728–742.

Iqbal, M. (1983), *An Introduction to Solar Radiation*, 390 pp., Academic Press, Toronto, New York.

Iwabuchi, H. (2006), Efficient Monte Carlo methods for radiative transfer modelling, *J. Atmos. Sci.*, *63*, 2324–2339.

Kawrakow, I., and D. W. O. Rogers (2001), The EGSnrc code system: Monte Carlo simulation and photon transport, NRCC Rep. PIRS-701, 287 pp.

Kazadzis, S., J. Grobner, A. Arola, and V. Amiridis (2010), The effect of global UV irradiance measurement accuracy on the single scattering albedo retrieval, *Atmos. Meas. Tech.*, *3*, 1029–1037.

Kokhanovsky, A. A., B. Mayer, V. V. Rozanov, K. Wapler, J. P. Burrows, and U. Schumann (2007a), The influence of broken cloudiness on cloud top height retrievals using nadir observations of backscattered solar radiation in the oxygen A-band, *J. Quant. Spectros. Radiat. Transfer*, *103*, 460–477.

Kokhanovsky, A. A., B. Mayer, V. V. Rozanov, K. Wapler, L. N. Lamsal, M. Weber, J. P. Burrows, and U. Schumann (2007b), Satellite ozone retrieval under broken cloud conditions: An error analysis based on Monte Carlo simulations, *IEEE Trans. GeoSci. Remote Sens.*, *45*(1), 187–194.

Koren, I., L. Oreopoulos, G. Feingold, L. A. Remer, and O. Altaratz (2008), How small is a small cloud?, *Atmos. Chem. Phys.*, *8*, 3855–3864.

Krzyscin, J. W., J. Jaroslawski, and P. S. Soboleswski (2003), Effects of clouds on the surface erythemal UV-B irradiance at northern midlatitudes: Estimation from the observations taken at Belsk, Poland (1999–2001), *J. Atmos. Sol. Terr. Phys.*, *65*, 457–467.

Kuchinke, C., and M. Núñez (1999), Cloud transmission estimates of UV-B erythemal irradiance, *Theor. Appl. Climatol.*, *63*, 149–161.

Kylling, A., A. Albold, and G. Seckmeyer (1997), Transmittance of a cloud is wavelength-dependent in the UV-range: Physical interpretation, *Geophys. Res. Lett.*, *24*, 397–400.

Loeb, N., T. Varnai, and R. Davies (1997), Effect of cloud inhomogeneities on the solar zenith angle dependence of nadir reflectance, *J. Geophys. Res.*, *102*, 9387–9395, doi:10.1029/96JD03719,1997.

Lovejoy, S., D. Schertzer, Y. Tessier, and H. Gaonach (2001), Multifractals and resolution-independent remote sensing algorithms: An example of ocean colour, *Int. J. Remote Sens.*, *22*, 1191–1234.

Lovengreen, C., H. Fuenzalida, and L. Videla (2005), On the spectral dependency of UV radiation enhancements due to clouds in Valdivia, Chile (39.8 S), *J. Geophys. Res.*, *110*, D14207, doi:10.1029/2004JD005372.

Lubin, D., and J. E. Frederick (1991), The ultraviolet radiation environment of the Antarctic Peninsula: The roles of ozone and cloud cover, *J. Appl. Meteorol.*, *30*, 478–491.

Marshak, A., S. Platnick, T. Várnai, G. Wen, and R. F. Cahalan (2006), Impact of 3D radiative effects on satellite retrievals of cloud droplet sizes, *J. Geophys. Res.*, *111*, DO9207, doi:10.1029/2005JD006686.

Mayer, B., and A. Kylling (2005), Technical note: The LibRadtran software package for radiative transfer calculations—Description and examples of use, *Atmos. Chem. Phys.*, *5*, 1855–1877.

McArthur, L. B. J. (2004), *Baseline Surface Radiation Network, Operations Manual, Version 2.1*, 176 pp., World Clim. Res. Programme, Geneva.

McCormick, P. G., and H. Suehrcke (1990), Cloud-reflected radiation, *Nature*, *345*, 773.

McPeters, R., M. Kroon, G. Labow, E. Brinksma, I. Petropavlovskikh, J. P. Veefkind, P. F. Bhartiam, and P. F. Levelt (2008), Validation of the Aura Ozone Monitoring Instrument total ozone product, *J. Geophys. Res.*, *113*, D15S14, doi:10.1029/2007JD008802.

Mims, F. M., and J. E. Frederick (1994), Cumulus clouds and UV-B, *Nature*, *371*, 391.

Minnis, P., P. W. Heck, D. F. Young, C. W. Fairall, and J. B. Snider (1992), Stratocumulus cloud properties derived from simultaneous satellite and island-based instrumentation during FIRE, *J. Appl. Meteorol.*, *31*, 317–339.

Molina, L. T., and M. J. Molina (1986), Absolute absorption cross-section of ozone in the 185 to 350 nm wavelength range, *J. Geophys. Res.*, *91*, 14,501–14,508.

Nikitidou, E., A. Kazantzidis, V. de Bock, and H. de Backer (2013), The aerosol forcing efficiency in the UV region and the estimation of single scattering albedo at a typical West European site, *Atmos. Environ.*, *69*, 313–320.

Núñez, M., M. J. Marín, M. P. Utrillas, V. Estellés, and J. A. Martínez-Lozano (2011), Incorporation of aerosol effects in a clear-sky semi-empirical model of UVER radiation for Valencia, Spain, *Int. J. Climatol.*, *31*, 937–948, doi:10.1002/joc.2133.

Núñez, M., M. P. Utrillas, and J. A. Martínez-Lozano (2012), Approaches to partitioning the global UVER irradiance into its direct and diffuse components in Valencia, Spain, *J. Geophys. Res.*, *117*, D02204, doi:10.1029/2011JD016087.

Parisi, A. V., J. Sabburg, and M. J. Kimlin (2004), Scattered and filtered solar UV measurements, *Adv. Global Change Res.*, vol. 17, Kluwer Acad., Dordrecht, Netherlands.

Petters, J. L., V. K. Saxena, J. R. Slusser, B. N. Wenny, and S. Madronich (2003), Aerosol single scattering albedo retrieved from measurements of surface UV irradiance and a radiative transfer model, *J. Geophys. Res.*, *108*(D9), 4288, doi:10.1029/2002JD002360.

Pfister, G., R. L. McKenzie, B. Liley, A. Thomas, C. N. Long, and B. N. Forgan (2003), Cloud coverage based on all-sky imaging and its impact on surface solar irradiance, *J. Appl. Meteorol.*, *42*, 1421–1434.

Press, W. H., B. P. Flannery, S. A. Teukolsky, and W. T. Vetterling (2007), *Numerical Recipes*, Cambridge Univ. Press, Cambridge.

Sabburg, J., and J. Calbó (2009), Five years of cloud enhanced surface UV radiation measurements at two sites (in Northern and Southern Hemispheres), *Atmos. Res.*, *93*, 902–912.

Sabburg, J., and J. Wong (2000), The effect of clouds in enhancing UVB irradiance at the Earth's surface: A one year study, *Geophys. Res. Lett.*, *27*, 3337–3340, doi:10.1029/2000GL011683.

Schafer, J. S., W. K. Saxena, B. N. Wenny, W. Barnard, and J. J. De Luisi (1996), Observed influence of clouds on ultraviolet-B radiation, *Geophys. Res. Lett.*, *23*, 2625–2628, doi:10.1029/96GL01984.

Serrano, D., M. Núñez, M. P. Utrillas, M. J. Marín, C. Marcos, and J. A. Martínez-Lozano (2014), Effective optical depth for overcast conditions determined with UV radiometers, *Int. J. Climatol.*, *34*(15), 3939–3952, doi:10.1002/joc.3953.

Shettle, E. P. (1989), Models of aerosols, clouds and precipitation for atmospheric propagation studiesin atmospheric propagation in the UV, visible, IR and mm-region and related system aspect, *AGARD Conf. Proc.*, *454*, 15–32.

Shettle, E. P., and R. W. Fenn (1979), Models for the aerosol lower atmosphere and the effects of humidity variations on their optical properties, *AFCRL Tech. Rep. 79 0214*, 100 pp., Air Force Cambridge Res. Lab., Hanscom Air Force Base, Mass.

Steyn, D. M. (1980), The calculation of view factors from fisheye lens photographs, *Atmos. Ocean.*, *18*, 254–258.

Thiel, S., K. Steiner, and H. K. Seldlitz (1997), Modification of global erythemally effective irradiance by clouds, *Photochem. Photobiol.*, *65*, 969–973.

Thuillier, G., M. Herse, D. Labs, T. Foujols, W. Peetermans, D. Gillotay, P. C. Simon, and H. Mandel (2003), The solar spectral irradiance from 200 to 2400 nm as measured by the SOLSPEC spectrometer from the SPEC spectrometer from the ATLAS and EURECA missions, *Sol. Phys.*, *214*, 1–22.

Twohy, C. H., J. A. Coakley Jr., and W. R. Tahnk (2009), Effect of changes in relative humidity on aerosol scattering near clouds, *J. Geophys. Res.*, *114*, D05205, doi:10.1029/2008JD010991.

Utrillas, M. P., M. J. Marín, A. R. Esteve, F. Tena, V. Estellés, and J. A. Martínez-Lozano (2007), Diffuse UV erythemal radiation experimental values, *J. Geophys. Res.*, *112*, D24207, doi:10.1029/2007JD008846.

Vandaele, A. C., C. Hermans, S. Fally, M. Carlee, M.-F. Merienne, A. Jenouvrier, C. Cocquart, and R. Colin (2003), Absorption cross-section of NO_2: Simulation of temperature and pressure effects, *J. Quant. Spectros. Radiat. Transfer*, *76*, 373–394.

Varnai, T., A. Marshak, and W. Yang (2013), Multi-satellite aerosol observations in the vicinity of clouds, *Atmos. Chem. Phys.*, *13*, 3899–3908.

Vilaplana, J. M., V. E. Cachorro, M. Sorribas, E. Luccini, A. M. de Frutos, A. Berjón, and B. de la Morena (2006), Modified calibration procedures for a Yankee Environmental Systems UVB-1 biometer based on spectral measurements with a Brewer spectrophotometer, *Photochem. Photobiol.*, *82*, 508–514.

Wielicki, B. A., and R. M. Welch (1986), Cumulus cloud properties derived using Landsat satellite data, *J. Appl. Meteorol.*, *25*, 261–276.

Wood, R. (2012), Stratocumulus clouds, *Mon. Weather Rev.*, *140*, 2374–2423.